J Clust Sci (2008) 19:295–309
DOI 10.1007/s10876-007-0175-0

COTTON MEMORIAL SPECIAL ISSUE

Linked Metal-cluster Systems: Isolation and Characterisation of {*anti*-[(*p*-cymene)RuCl]-μ-[κ^2-*P*,*P*′;κ^1-*P*″-$(PPh_2CH_2)_3$CMe]-$[AuPt_3(CO)_3(PCy_3)_3]$}$(PF_6)_2$

Adrian B. Chaplin · Zoltán Béni · Christian G. Hartinger · Hisham Ben Hamidane · Andrew D. Phillips · Rosario Scopelliti · Paul J. Dyson

Received: 22 October 2007 / Published online: 18 December 2007

Abstract The new mixed-metal complex {*anti*-[(*p*-cymene)RuCl]-μ-[κ^2-*P*,*P*′;κ^1-*P*″-$(PPh_2CH_2)_3$CMe]-[AuCl]}PF_6 and its cluster derivative {*anti*-[(*p*-cymene)RuCl]-μ-[κ^2-*P*,*P*′;κ^1-*P*″-$(PPh_2CH_2)_3$CMe]-$[AuPt_3(CO)_3(PCy_3)_3]$}$(PF_6)_2$ have been prepared and characterized. Notably, NMR spectroscopy and high resolution FT-ICR mass spectrometry, including a tandem mass spectrometric analysis, demonstrated the formation of these compounds that was also confirmed by single crystal X-ray diffraction analysis.

Keywords Clusters · Heteronuclear clusters · Platinum · X-ray structures

Introduction

Recent years have witnessed the emergence of many systematic synthetic approaches in cluster chemistry in which predictable products are isolated in high yields [1]. Of course, the complexity of cluster compounds makes such a goal more difficult to achieve than for related chemistry involving mononuclear compounds.

In metal carbonyl clusters, reagents such as trimethylamine *N*-oxide allow the sequential substitution of CO ligands by other ligands of choice, although it should be noted that the site of substitution is often difficult to predict [2]. Much success in the rational synthesis of clusters has been made in the domain of heteronuclear systems, usually with the metal fragment being condensed onto a central cluster unit [3]. Adams has recently employed the 14 VE complex $Pt(P^tBu_3)_2$, and the palladium analogue, to produce an array of new heteronuclear clusters (see Scheme 1 for some examples) [4].

A. B. Chaplin · Z. Béni · C. G. Hartinger · H. B. Hamidane · A. D. Phillips · R. Scopelliti · P. J. Dyson (✉)
Institut des Sciences et Ingénierie Chimiques, Ecole Polytechnique Fédérale de Lausanne (EPFL), CH-1015 Lausanne, Switzerland
e-mail: paul.dyson@epfl.ch

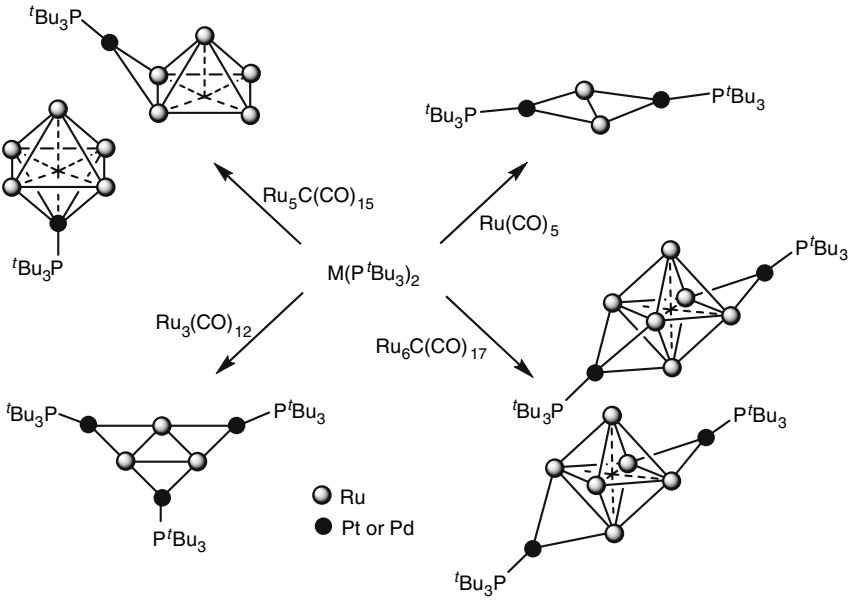

Scheme 1 Examples of condensation reactions between the reactive 14 VE complex $M(P^tBu_3)_2$ (M = Pd or Pt) and various ruthenium carbonyl compounds recently reported by Adams and co-workers (CO ligands omitted for clarity)

Other useful reagents have been reported previously, and notably, mercury reagents have been employed as a type of 'universal glue' [5] and gold phosphine fragments [6], which are isolobal with hydrides [7], readily replacing them in many structures.

Relatively little attention has been directed towards the synthesis of clusters with tethered monometallic fragments, however, one notable example is the use of 1,1'-bis(diphenylphosphino)ferrocene (dppf) [8], in which the cluster unit has been shown to communicate with the iron centre in the chelating phosphine ligand [9]. Other bis-phosphines have also been shown to bridge single metal complexes and cluster compounds [10], and the reverse notion, i.e. that of clusters acting as ligands has even been suggested [11]. Nevertheless, well defined examples of cluster-complex tethers not based on the bis-phosphine ligands are rare and in this paper we provide an example of a very well characterised example based on the triphos ligand.

Results and Discussion

Synthesis

Reaction of the known half sandwich ruthenium(II)-arene complex containing a partially coordinated tripodal phosphine ligand (triphos), *anti*-[RuCl(κ^2-$(PPh_2CH_2)_3$-CCMe)(*p*-cymene)]PF_6 **1**.PF_6 [12], with [AuCl(SC_4H_8)], affords the corresponding

bimetallic ruthenium(II)-gold(I) complex **2**.PF_6, by substitution of the labile tetrahydrothiophene ligand by the pendant phosphine moiety, in good yield (79%, Scheme 2). The formation of the gold adduct is readily confirmed by a characteristic shift to higher frequency of the pendant phosphine moiety in **1** from −28 to 16 ppm in **2**.PF_6 by ^{31}P NMR spectroscopy. Further verification of this complex is provided by solid-state characterisation and ESI-FT-ICR-MS experiments (see below). Complex **2**.PF_6 serves as a convenient precursor to the synthesis of linked ruthenium(II)-cluster systems by chloride abstraction from the gold(I) centre followed by reaction with an appropriate cluster. Thus, reaction of **2**.PF_6 with the Lewis basic triplatinum phosphine cluster $[Pt_3(CO)_3(PCy_3)_3]$ in the presence of $TlPF_6$, as a chloride abstracting agent, at room temperature affords the triphos linked ruthenium (II)-cluster complex, {*anti*-[(*p*-cymene)RuCl]-μ-[κ^2-*P*,*P*′;κ^1-*P*″-$(PPh_2CH_2)_3CMe$]-$[AuPt_3(CO)_3(PCy_3)_3]$}$(PF_6)_2$ **3**.$(PF_6)_2$, in good yield (77%, Scheme 2). The structure of **3** is unambiguously assigned on the basis of $^{31}P\{^1H\}$ NMR and IR spectroscopy, mass spectroscopy and X-ray diffraction analysis, which are discussed in detail below. Compound **3**.$(PF_6)_2$ is air-stable in the solid-state and shows no discernable reaction on standing in solution over long periods of time (ca. >1 week in CD_2Cl_2). Exchange of the cluster moiety is observed in the presence of excess $[Pt_3(^{13}CO)_3(PCy_3)_3]$ in THF at 60 °C by ^{13}C NMR spectroscopy, although this process is negligible at RT in CD_2Cl_2.

Spectroscopic Characterisation

The ^{31}P NMR spectrum of **3**.$(PF_6)_2$ in CD_2Cl_2 at 20 °C exhibits characteristic coupling patterns which confirm the proposed structure (Fig. 1). The NMR spectra of polynuclear platinum species are complicated by the distribution of ^{195}Pt isotopes (natural abundance 33.7%). Accordingly, spectra are observed as superimpositions of signals from different isotopomers present in solution; in this case, species with 0, 1, 2, or 3 ^{195}Pt nuclei in the cluster skeleton. Consequently, the ^{31}P NMR spectrum

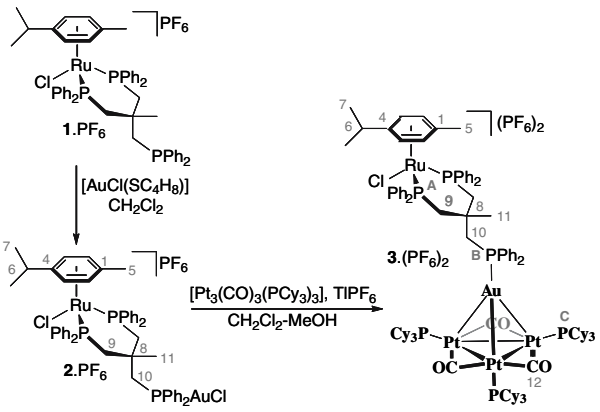

Scheme 2 Synthetic route to **2**.PF_6 and **3**.$(PF_6)_2$ (including NMR labelling schemes)

of **3**.$(PF_6)_2$ cannot be analysed in the first order and simulation of the spectra (using gNMR) was carried out in order to extract spectral parameters (results are listed in Table 1, with the corresponding simulated spectra depicted in Fig. 1). The triphos resonance $P^{\mathbf{A}}$ (see Scheme 2 for labelling) is observed as broad singlet at 29.4 ppm ($w_{1/2}$ 143 Hz) at similar frequency to that in **2**.PF_6 (28.7 ppm), whereas the triphos resonance $P^{\mathbf{B}}$ is shifted to much higher frequency in comparison to **2**.PF_6 (41.9 vs. 15.5 ppm) and is observed as a quartet with platinum satellites; confirming the symmetrical nature of gold binding to the cluster adduct. The tricyclohexylphosphine resonance $P^{\mathbf{C}}$ is centred at 54.7 ppm, to lower frequency than that of the starting complex (69.8 ppm) [13] and is similar to related PR_3Au-adducts of $[Pt_3(CO)_3(PCy_3)_3]$ (52.2–58.1 ppm); the observed coupling constants are also in good agreement with these adducts [14].

Progressive cooling of the sample to −80 °C results in the resolution of the $P^{\mathbf{A}}$ resonance into a pair of doublets at 38.6 and 20.1 ppm with a $^2J_{PP}$ coupling constant of 65 Hz, indicative of a fluxional process of the triphos ligand coordinated to the ruthenium(II) centre (Fig. 2). This is presumably due to the large degree of steric bulk on the third triphos arm causing conformational changes to the metallacyclic ring (see below). In agreement with this suggestion the line broadening at ambient temperature of the ruthenium coordinated triphos resonances decreases in the order

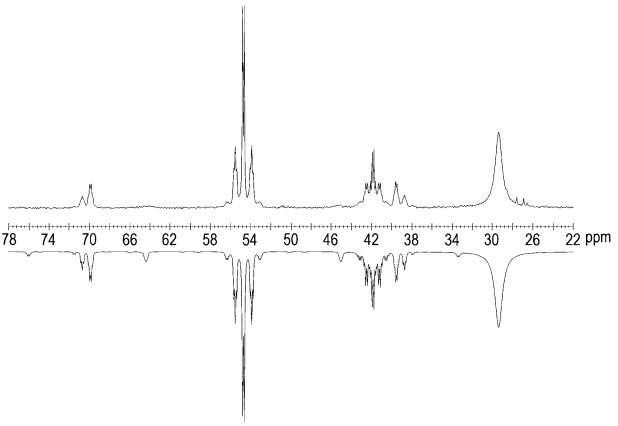

Fig. 1 Observed (above) and simulated (below) $^{31}P\{^1H\}$ NMR spectra of **3**.$(PF_6)_2$ (CD_2Cl_2, 20 °C)

Table 1 ^{31}P NMR chemical shifts and coupling constants for **3**.$(PF_6)_2$ obtained by simulation analysis (excluding anion resonance) [15]

	δ/ppm	$w_{1/2}$/Hz	J/Hz
$P^{\mathbf{A}}$	29.4	143	
$P^{\mathbf{B}}$	41.9	13	$^3J_{\mathbf{BC}} = 28$, $^2J_{\mathbf{BPt}} = 209$
$P^{\mathbf{C}}$	54.7	13	$^3J_{\mathbf{CC'}} = 21$, $^1J_{\mathbf{CPt}} = 4916$, $^2J_{\mathbf{CPt}} = 265$
			$^1J_{\mathbf{PtPt'}} = -1886$

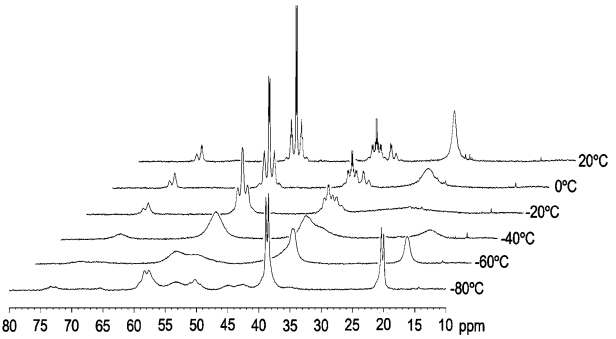

Fig. 2 Variable temperature $^{31}P\{^{1}H\}$ NMR spectra of **3**.$(PF_6)_2$ in CD_2Cl_2

3.$(PF_6)_2 \gg$ **2**.PF_6 (30 Hz) > **1**.PF_6 (10 Hz). The P^{B} and P^{C} resonances also undergo change upon cooling, resolution is not achieved at −80 °C, and the origin of this comparably more rapid dynamic behaviour is unclear.

In the IR spectrum of **3**.$(PF_6)_2$ (CH_2Cl_2 solution) a single strong carbonyl absorption band at 1807 cm^{-1} is observed, 43 cm^{-1} to higher frequency than that observed in $[Pt_3(CO)_3(PCy_3)_3]$. This shift to higher frequency is consistent with the reduced π-basicity of the cluster as a result of the capping of the gold phosphine adduct. Similar shifts to higher frequency are observed for related PR_3Au-adducts of $[Pt_3(CO)_3(PCy_3)_3]$ (ca. 30 cm^{-1}) [14].

Electrospray Ionisation Mass Spectrometry Study

Electrospray ionisation mass spectrometry has been shown to be a valuable tool for characterizing clusters [16] and was also shown to be suitable for studying the interactions of metal complexes with other high molecular weight compounds such as proteins [17–19].

The full scan FT-ICR mass spectra of **2**.PF_6 and **3**.$(PF_6)_2$ contained the expected peaks for the two species resulting from the cluster cations: a singly charged species at *m/z* 1127 was assigned to **2** and a doubly charged isotope cluster at *m/z* 1301 correlates with **3** (see Fig. 3). The calculated and recorded isotope patterns show excellent correlation, and notably, the soft ionisation conditions resulted in no fragmentation of these species.

In order to obtain structural information on the two compounds and for estimating relative stabilities, MS^n experiments were performed utilizing both the ion trap (IT) and the high resolution Fourier-transform ion cyclotron resonance (FT-ICR) as analysers (Fig. 4). An MS^2 experiment for **3**, employing collision-induced dissociation (CID), revealed the formation of a doubly charged species at *m/z* 1259 assignable to [**3**–3 CO]$^{2+}$ which was further fragmented (MS^3) to [**3**–{(*p*-cymene)$RuCl(PPh_2CH_2)_3CMe$}–3 CO–H]$^+$ (*m/z* 1621), [(*p*-cymene)$RuCl(PPh_2CH_2)_3CMe]^+$ (*m/z* 895), and $[RuCl(PPh_2CH_2)_3CMe]^+$ (*m/z* 761). An MS^4 experiment on [(*p*-cymene)$RuCl(PPh_2CH_2)_3CMe]^+$ (*m/z* 895) gave exclusively $[RuCl(PPh_2CH_2)_3CMe]^+$ (*m/z* 761) which further fragmented, initiated by CID, to

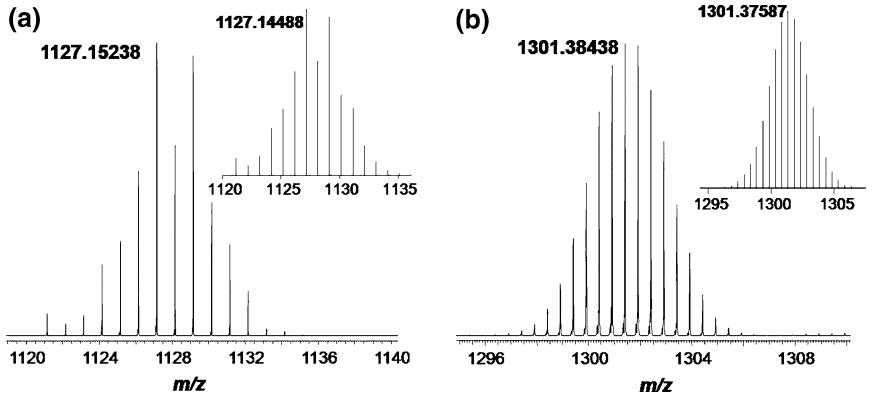

Fig. 3 Recorded FT-ICR mass spectrum and (inset) theoretical isotope patterns of (**a**) **2** and (**b**) **3**

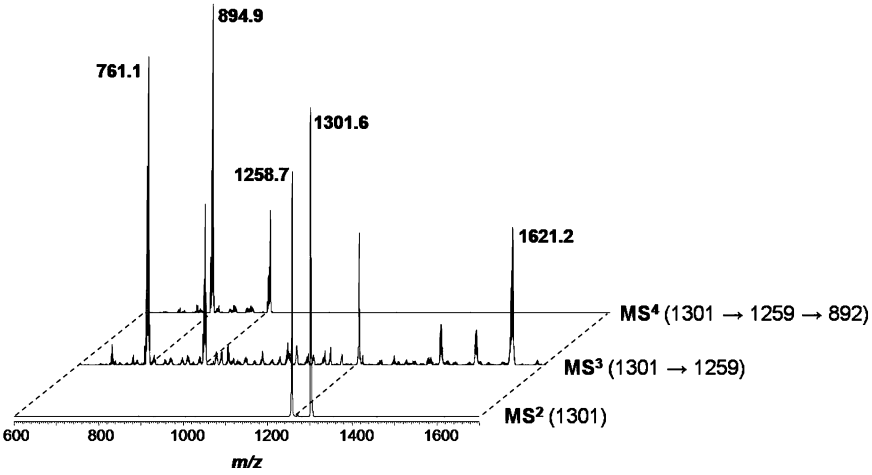

Fig. 4 MS^n obtained by CID of **3**

daughter ions resulting from the loss of the chloro ligand and cleavage of the phosphine ligand. In general, the same fragments were observed by FT-ICR-MS.

The full scan mass spectra recorded in ion trap and FT-ICR mode of **2** contain single peaks at ca. *m/z* 1127, which can be fragmented by CID to *m/z* 993. The latter peak can be assigned to $[\mathbf{2}–\{\text{p-cymene}\}]^+$ which can be transformed by MS^3 to *m/z* 761, although this peak shows an inconclusive isotope pattern. When performing the tandem MS experiments with the ion trap a species with *m/z* 761 is obtained showing that both **2** and **3** fragment to the same daughter ion. This experiment also indicates that this species is a very stable fragment surviving a manifold of collisions in contrast to the Au–Pt cluster of **3**. Further fragmentation experiments of the daughter ion of **2** at *m/z* 761 resulted in the same fragments as for **3**.

Crystallographic Characterisation

Molecular structures of **2**.PF_6 and **3**.$(PF_6)_2$ were obtained by single crystal X-ray diffraction and are shown in Figs. 5 and 6, respectively. The anti-configuration of the triphos-ligand in the structure of **2**.PF_6 is readily observable and the cation is accompanied by an equatorial disordered PF_6 counter-anion and two chloroform solvates. The coordination of the third triphos arm to the Au(I) center in **2**.PF_6 occurs with an essentially linear P–Au–Cl arrangement [177.11(8)°] in good agreement with that found for gold phosphine complexes such as Ph_3PAuCl [20]. There are three crystal structures reported in which one arm of the triphos ligand is bound to a Au–Cl fragment, while the remaining two phosphorus centers are chelating a transition metal or metal-ligand fragment (fragment = Au [21], $Mo(CO)_4$ [22], and $PtCl_2$ [23]), although the metric parameters for the $PtCl_2$ containing complex are less reliable due to a mixture of Au–Cl and Au–Br components present in the unit cell [23]. A comparison of the relevant bond lengths and angles for these compounds and **1**.PF_6, **2**.PF_6 and **3**.$(PF_6)_2$ is provided in Table 2, and key bond lengths for **1**.PF_6, **2**.PF_6 and **3**.$(PF_6)_2$ are collated in Table 3. In general, only slight variations in the triphos–Au–Cl geometries are observed among this series, except for the C–CH_2–P(Ph_2)–Au torsion angle which shows sizeable differences amongst the complexes, suggesting a large degree of rotational flexibility of the triphos arm coordinated to the Au center (or pendant phosphine arm). A shortening of the P–C(H_2) bond is observed for complex **2**.PF_6 [1.824(6) Å] as compared to **1**.PF_6 [1.853(4) Å] [12] and the free triphos ligand [1.853(6), 1.859(5), 1.861(5) Å] [24]. Interestingly, only a slight change between **2**.PF_6 and

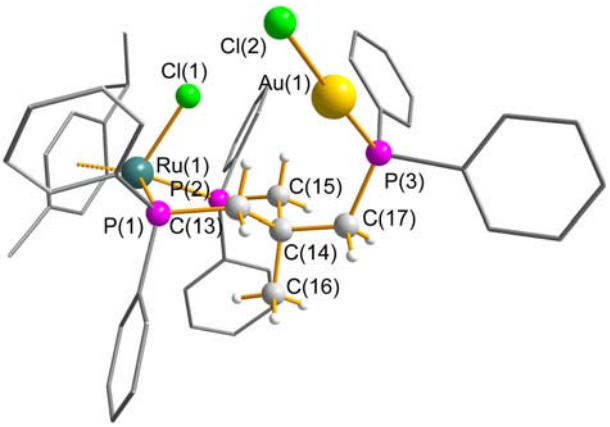

Fig. 5 Ball-and-Stick diagram of compound **2**.PF_6 showing the chair-conformation of the Ru–triphos ring system. Counter-ion and solvates have been removed for clarity. Selected bond lengths (Å) and angles (°): Ru1–C(ring) average 2.23, Ru1–Cl1 2.392(2), Ru1–P1 2.335(2), P1–C13 1.831(6), Ru1–P2 2.349(2), P2–C16 1.841(6), C13–C14 1.527(8), C14–C16 1.538(8), C14–C17 1.572(8), P3–C17 1.824(6), P3–Au1 2.232(2), Au1–Cl2 2.285(2). P1–Ru1–P2 89.58(6), Cl1–Ru–P1 81.07(6), Cl1–Ru–P2 84.72(6). Ru1–P1–C13 116.2(2), P1–C13–C14 119.1(5), C13–C14–C15 113.0(5), Ru1–P2–C15 115.2(2), P2–C15–C14 118.4(4), C16–C14–C17 103.9(4), C14–C17–P3 121.2(4), C17–P3–Au1 117.8(2), P3–Au1–Cl2 177.11(8)

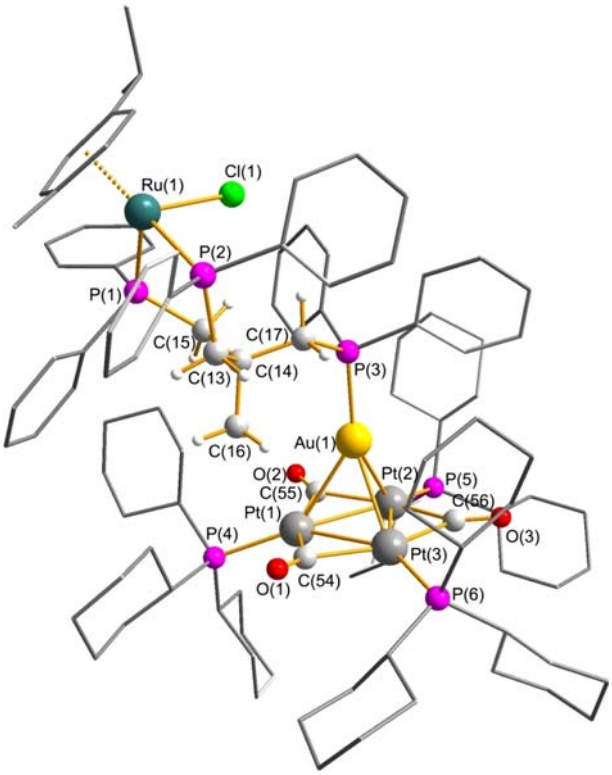

Fig. 6 Ball-and-Stick diagram of **3**.$(PF_6)_2$ showing the chair-conformation of the Ru–triphos ring system and the orientation of the Au–Pt cluster. Counter-ions and solvates have been removed for clarity. Selected bond lengths (Å) and angles (°): Ru1–C(ring) average 2.28, Ru1–Cl1 2.407(4), Ru1–P1 2.333(3), Ru1–P2 2.326(4), P1–C13 1.86(2), P2–C15 1.84(1), C15–C14 1.55(2), C13–C14 1.55(2), C14–C16 1.53(2), C14–C17 1.54(2), C17–P3 1.88(2), P3–Au1 2.264(3), Au1–Pt1 2.7411(7), Au1–Pt2 2.7793(6), Au1–Pt3 2.7591(6), Pt1–Pt2 2.6823(8), Pt1–Pt3 2.6862(8), Pt2–Pt 2.6894(8), Pt1–P4 2.280(4), Pt2–P5 2.287(4), Pt3–P6 2.288(4), Pt1–C54 2.112(4), Pt3–C54 2.093(13), Pt3–C56 2.066(13), C56–Pt2 2.071(15), Pt2–C55 2.075(4), C55–Pt1 2.060(15), C54–O1 1.149(17), C55–O2 1.16(2), C56–O3 1.162(18). Cl1–Ru1–P1 83.05(12), Cl1–Ru1–P2 86.80(13), P1–Ru1–P2 88.29(12), Ru1–P1–C13 116.2(5), Ru1–P2–C15 86.80(13), P1–C13–C14 118.6(9), C13–C14–C15 114.8(11), P2–C15–C14 114.8(4), C16–C14–C17 111.8(11), C14–C17–P3 122.0(9), C17–P3–Au1 115.4(4), P3–Au1–Pt1 146.23(9), P3–Au1–Pt2 145.82(10), P3–Au–Pt3 145.39(9), Pt1–Au1–Pt2 58.14(12), Pt2–Au1–Pt3 58.10(2), Pt1–Au1–Pt3 58.47(2), Pt1–Pt2–Pt3 60.01(2), Pt2–Pt3–Pt(1) 59.87(2), P3–Pt1–Pt2 60.13(2), Au1–Pt1–P5 134.83(8), Au1–Pt2–P4 142.79(9), Au1–Pt3–P6 135.53(9), Pt2–C53–Pt1 81.0(6), Pt1–C54–Pt2 79.3(5), Pt2–C52–Pt3 81.1(5)

1.PF_6 is noted for the P–C(H_2)–C(Me) bond angle and the three angles around the phosphorus center (C(H_2)–P–(C)Ph and (Ph(C)–P–C(Ph)). The C(H_2)–C(Me)–C(H_2)–P(Au/none) torsion angles are significantly different in the two complexes, **1**.PF_6 [71.9(3)° and 141.3(3)°] and **2**.PF_6 [-56.2(6)° and 66.6(6)°]. In fact, the linear P–Au–Cl unit is positioned such that it slightly eclipses one phenyl group of the chelating phosphines. A comparison of the metric parameters about the Ru center in **1**.PF_6 and **2**.PF_6 reveals identical arene and chlorine distances with and without Au–Cl coordination. However, differences in the P–Ru–P bond angle are present,

Table 2 Selected bond lengths (Å), angles (°) and torsion angles (°) for the P–Au–Cl fragment in **1**.PF_6, **2**.PF_6, **3**.$(PF_6)_2$ and related gold(I) chloride triphos transition metal complexes[a]

	Au–X	P–Au	P–Au–Cl	$C(H_2)$–P	$C(H_2)$–P–Au	C(R)–$C(H_2)$–P–Au	Ref.
1.PF_6	n/a	n/a	n/a	1.853(4)	n/a	n/a	[12]
2.PF_6	2.285(2)	2.232(2)	177.11(8)	1.824(6)	117.8(2)	58.8(5)	
3.$(PF_6)_2$	n/a	2.264(3)	n/a	1.88(2)	115.4(4)	n/a	
L-$Mo(CO)_4$	2.286(3)	2.231(3)	177.42(13)	1.838(5)	117.6(2)	−46.1(5)	[22]
L-$PtCl_2$	n/a	2.238(3)	n/a	1.816(12)	116.7(4)	33.8(10)	[23]
L-Au[b]	2.273(11)	2.251(16)	178.3(5)	1.80(1)	117(1)	45.18(2)	[21]
	2.292(11)	2.212(11)	177.9(5)	1.72(2)	116(1)	−50(3)	
	2.319(14)	2.213(16)	178.5(4)	1.79(4)	116(1)	50(2)	
	2.267(11)	2.243(10)	177.7(4)	1.86(2)	116(1)	−56(3)	

[a] L = triphos gold moiety

[b] Two crystallographically independent molecules present within the unit cell

Table 3 Key bond lengths (Å) and angles (°) around the ruthenium centre in complexes **1**.PF_6, **2**.PF_6 and **3**.$(PF_6)_2$

	Ru–Cl	Ru–P	Ru–C(ring) av.	P–Ru–P	P–Ru–Cl	Ref
1.PF_6	2.390(1)	2.336(1)	2.28	86.92(4)	84.94(4)	[12]
		2.331(1)			88.32(4)	
2.PF_6	2.392(2)	2.335(2)	2.23	89.58(6)	81.07(6)	
		2.349(2)			84.72(6)	
3.$(PF_6)_2$	2.407(4)	2.333(3)	2.28	88.29(12)	83.05(12)	
		2.326(4)			82.99(9)	

which appear to originate from a twisting of the triphos P–$C(H_2)$–C(Me)–$C(H_2)$–P backbone. For example, in **1**.PF_6, the two P(Ru)–$C(H_2)$–C(Me)–$C(H_2)$ torsion angles differ substantially [3.1(4)°, 58.7(4)°], whereas in **2**.PF_6, and compounds of the type $M(PPh_2CH_2)_2CMe(CH_2PPh_2AuCl)$ (M=Au, $Mo(CO)_4$, $PtCl_2$), such torsion angles are equivalent within experimental error [**2**.PF_6: 65.3(6)° and −66.5(6)°]. The chair configuration of the Ru–triphos ring is required to accommodate coordination of the Au–Cl fragment to the phosphorus, resulting in a narrowing of angle corresponding to the central carbon of the triphos ligand, [cf. **1**.PF_6 110.2(3)° vs. **2**.PF_6 103.9(4)°].

The structure of **3**.$(PF_6)_2$ features the ruthenium–arene triphos moiety κ^1-coordinated to the gold center which in turn caps an equilateral planar cluster comprising three Pt(PCy_3) units intra-molecularly connected by μ^2-bridging CO ligands. For this structure, two non-disordered PF_6 counter-ions are present along with multiple chloroform solvates. Both the Au–P [2.264(3) Å] and P(Au)–$C(H_2)$ [1.876(14) Å] distances are longer than those in species **2**.PF_6 and reflect the higher coordination number of the Au center. All three Pt–Pt distances are similar [2.682(1), 2.689(1), 2.686(1) Å], however, some distortion is observed in the Au–Pt distances [2.741(1), 2.779(1), 2.759(1) Å] with a minor shortening to one side of the

cluster, which is not reflected in the Pt–P(Cy_3) bond distances [2.286(4), 2.288(4) and 2.287(4) Å]. Compared with those of [$Pt_3(CO)_3(PCy_3)_3$] [25] and 1,4-μ_2-(C_6H_4)($CH_2PPh_2Au[Pt_3(CO)_3(PCy_3)_3]$)$_2$ [14], the Pt–Pt distances in **3**.(PF_6)$_2$ are only slighter longer, see Table 4. However, the Au–Pt distances in the bridging phosphine species (1,4-μ_2-(C_6H_4)-($CH_2PPh_2Au[Pt_3(CO)_3(PCy_3)_3]$)$_2$) indicate a greater degree of distortion than that found in **3**.(PF_6)$_2$, which is probably due to greater steric demands of the C_6H_4–CH_2PPh_2 fragment over the pendant phosphine arm of triphos, P(Ph_2)CH_2. The Pt–C(O) bridging bond lengths also are uneven, with one set showing significantly longer distances than the other two. Moreover, this feature is less dramatic than in {1,4-μ_2-(C_6H_4)-($CH_2PPh_2Au[Pt_3(CO)_3(PCy_3)_3]$)$_2$}. An examination of the metric parameter pertaining to the ruthenium–arene triphos fragment (Table 3) shows that the overall geometry is more comparable to the free-pendant species **1**.PF_6 than the AuCl coordinated complex **2**.PF_6. In particular, the triphos ligand is asymmetrically distorted as in **1**.PF_6, and does not feature the chair-conformation found in **2**.PF_6. This is shown by the differing P(Ru)–C(H_2)–C(Me)–C(H_2PRu) torsion angles; −3.2(15)° and −56.4 (15)°, similar to those in **1**.PF_6, and gives rise to slightly unequal Ru–P bond distances: 2.333(3) and 2.326(4) Å and much a wider angle at the central triphos carbon [111.8(11)°]. The adoption of the puckered triphos ring geometry can be inferred from the very high steric demands of the [Au–$Pt_3(CO)_3(PCy_3)_3$] component, but despite the bulk of the appended metal cluster, the C(R)–C(CH_2)–P–Au torsion angle are very similar in both **2**.PF_6 [58.8(5)°] and **3**.(PF_6)$_2$ [53.6(11)°].

To conclude, the strategy described herein to appendage metal fragments to cluster units via the triphos ligand could easily be extended to a broad range of metal/cluster systems. It is possible that such systems could be extended to produce novel inorganic polymers with interesting electrical or magnetic properties. We are currently preparing a more extensive range of compounds related to **3** and intend to explore their chemistry in greater depth.

Experimental Section

All manipulations were carried out under a nitrogen atmosphere using standard Schlenk techniques. CH_2Cl_2 was dried under nitrogen using a solvent purification system, manufactured by innovative technology inc. CD_2Cl_2 was distilled from CaH_2 and stored under nitrogen. All other solvents were p.a. quality and saturated with nitrogen prior to use. [AuCl(SC_4H_8)] [26] and [$Pt_3(PCy_3)_3(CO)_3$] [27] were prepared as described elsewhere. *anti*-[RuCl(κ^2-(PPh_2CH_2)$_3$CCMe)(*p*-cymene)]PF_6 was prepared by a minor modification to the original procedure that allowed this isomer to be separated in a pure form (as it is has lower solubility) [12]. All other chemicals are commercial products and were used as received. NMR spectra were recorded on a Bruker Avance 400 MHz spectrometer at room temperature, unless otherwise stated. IR spectra were recorded on a PerkinElmer Spectrum GX FT-IR spectrometer. Chemical shifts are given in ppm and coupling constants (J) in Hz. Simulation analysis of the $^{31}P\{^1H\}$ NMR spectrum of **3**.(PF_6)$_2$ was carried out using *g*NMR [28]. Microanalyses were performed at the EPFL.

Table 4 Key bond lengths (Å) and angles (°) for $[Pt_3(CO)_3(PCy_3)_3]$, 1,4-$(C_6H_4)(CH_2PPh_2Au[Pt_3(CO)_3(PCy_3)_3])_2$ and **3**.$(PF_6)_2$

	Pt–Pt	Pt–P	Pt–C	C–O	Au–Pt	Pt–Pt–Pt	Pt–C–Pt	Pt–Au–Pt	Ref
$[Pt_3(CO)_3(PCy_3)_3]$	2.656(2)	2.267(7)	2.06(4)	1.19(4)	n/a	59.9(1)	78.9(2)	n/a	[25]
	2.653(2)	2.282(9)	2.21(3)	1.16(4)	n/a	60.0(1)			
1,4-μ_2-$(C_6H_4)(CH_2PPh_2$	2.665(2)	2.273(4)	2.05(2)	1.18(2)	2.767(3)	60.14(7)	79.5(6)	58.02(7)	[14]
$Au[Pt_3(CO)_3(PCy_3)_3])_2$	2.662(2)	2.269(4)	2.04(2)	1.16(2)	2.728(3)	59.98(7)	81.5(6)	58.36(7)	[14]
	2.669(2)	2.280(4)	2.04(2)	1.21(2)	2.733(3)	59.89(7)	80.6(6)	58.07(7)	
			2.07(1)						
			2.08(1)						
			2.09(1)						
3.$(PF_6)_2$	2.682(1)	2.280(4)	2.09(1)	1.15(2)	2.741(2)	60.01(2)	81.0(6)	58.14(12)	
	2.686(1)	2.287(4)	2.07(1)	1.16(2)	2.779(1)	59.87(2)	79.3(5)	58.10(2)	
	2.689(1)	2.288(4)	2.07(2)	1.16(2)	2.759(1)	60.13(2)	81.1(5)	58.47(2)	
			2.06(2)						
			2.08(1)						
			2.11(1)						

Preparation of {*anti*-[(*p*-cymene)RuCl]-μ-[κ^2-*P*,*P*′;κ^1-*P*″-(PPh_2CH_2)$_3$CMe]-[AuCl]}PF_6 (**2**.PF_6)

A solution of *anti*-[RuCl(κ^2-(PPh_2CH_2)$_3$CCMe)(*p*-cymene)]PF_6 (0.080 g, 0.077 mmol) and [AuCl(SC_4H_8)] (1 eqv.) in CH_2Cl_2 (10 mL) was stirred at RT for 60 min. The product was precipitated by addition of excess hexane and isolated by filtration, washing with hexane (2 × 10 mL). Yield: 0.077 g (79%) as a yellow-orange powder. Yellow crystals suitable for X-ray diffraction were obtained from slow diffusion of pentane into a $CHCl_3$ solution of the complex. ^{1}H NMR (CD_2Cl_2, 400 MHz): δ 7.32–7.74 (m, 30H), 5.80 (d, $^3J_{HH} = 5.6$, 2H, $H^{3/2}$), 5.53 (d, $^3J_{HH} = 5.6$, 2H, $H^{2/3}$), 3.54–3.70 (m, 2H, H^9), 2.64 (m, d, $^2J_{PH} = 12$, 2H, H^{10}), 2.23–2.36 (m, 2H, $H^{9'}$), 2.20 (sept, $^3J_{HH} = 6.8$, 1H, H^6), 1.41 (s, 3H, H^5), 0.83 (d, $^3J_{HH} = 6.8$, 6H, H^7), 0.58 (s, 3H, H^{11}). ^{31}P{^{1}H} NMR (CD_2Cl_2, 162 MHz): δ 28.7 (s, 2P, Ru–$\underline{P}Ph_2$), 15.5 (s, 1P, $\underline{P}Ph_2$–AuCl), −144.3 (sept, $^1J_{PF} = 711$, 1P, $\underline{P}F_6$). Anal. Calcd. for $C_{51}H_{53}AuCl_2F_6P_4Ru$ (1272.81 gmol^{-1}): C, 48.13; H, 4.20. Found: C, 48.09; H, 4.32.

Preparation of {*anti*-[(*p*-cymene)RuCl]-μ-[κ^2-*P*,*P*′;κ^1-*P*″-(PPh_2CH_2)$_3$CMe]-[$AuPt_3(CO)_3(PCy_3)_3$]}$(PF_6)_2$ (**3**.$(PF_6)_2$)

A suspension of {*anti*-[(*p*-cymene)RuCl]-μ-[κ^2-*P*,*P*′;κ^1-*P*″-(PPh_2CH_2)$_3$CMe]-[AuCl]}PF_6 (0.043 g, 0.034 mmol), [$Pt_3(CO)_3(PCy_3)_3$] (1 eqv.) and $TlPF_6$ (2 eqv.) in CH_2Cl_2–MeOH (4:1 v/v, 25 mL) was stirred at RT for 60 min. The solvent was removed in vacuo and the residue extracted with CH_2Cl_2–Hexane (10:1 v/v, 22 mL) through celite. The product was then precipitated, as a orange-brown powder, by addition of excess hexane to the filtrate. Yield: 0.076 g (77%). Red crystals suitable for X-ray diffraction were obtained from slow diffusion of pentane into a $CHCl_3$ solution of the complex. ^{1}H NMR (CD_2Cl_2, 400 MHz): δ 6.94–7.79 (m, 30H), 5.77 (d, $^2J_{HH} = 5$, 2H, $H^{3/2}$), 5.40 (br 2H, $H^{2/3}$), 0.64–2.75 (m, 118H). ^{13}C{^{1}H} NMR (CD_2Cl_2, 100 MHz, selected peak only): δ 246.6 (s, $\underline{C}O$). ^{31}P{^{1}H} NMR (CD_2Cl_2, 162 MHz): δ 54.7 (m, 3P, Pt-$\underline{P}Cy_3$), 41.9 (m, 1P, Au–$\underline{P}Ph_2$), 29.4 (br, 2P, Ru–$\underline{P}Ph_2$), −144.3 (sept, $^1J_{PF} = 713$, 2P, $\underline{P}F_6$). IR(CH_2Cl_2): ν(CO) = 1,807 (vs) cm^{-1}. Anal. Calcd. for $C_{108}H_{152}AuClF_{12}O_3P_8Pt_3Ru$ (2892.89 gmol^{-1})·5(CH_2Cl_2): C, 40.91; H, 4.92. Found: C, 40.65; H, 5.01.

Mass Spectrometry

For electrospray ionisation mass spectrometry, 0.25 μM solutions of the isolated clusters were prepared in methanol (*p.a.*, Merck; LC-MS grade, Riedel-de Haën). The samples were placed into a 386-well plate in an Advion TriVersa^{TM} Nanomate equipped with a 5.5 μm-nozzle chip. The Nanomate was controlled with ChipSoft v7.2.0 software and the following parameters were set: gas pressure, 0.30 psi; voltage, 1.40 kV; sample volume, 10.00 μL. The samples were analysed using a hyphenated ion-trap–FT-ICR mass spectrometric system which

consisted of an LTQ XL and a 12 T FT-ICR-MS (both ThermoFisher Scientific, Bremen) in positive ion mode. The spectra were calibrated externally with substance P ($[H_2N\text{-RPKPQQFFGLM-}NH_2 + 2H]^{2+}$, *m/z* 674.37135; BACHEM, Switzerland). The Xcalibur software bundle was utilized for recording (Tune Plus version 2.2 SP1; ThermoFisher Scientific, Bremen) and data analysis (Qual Browser version 2.2; ThermoFisher Scientific, Bremen). All different stages of MS^n were done in the linear ion trap and the product ions were consecutively injected into the ICR cell. For MS^n the most abundant ions were selected at the MS^{n-1} stages and fragmentation was initiated by CID. For comparison purposes, both the ion trap and the FT-ICR analysers were used for detection of daughter ions.

Crystallography

Crystals were removed from the crystallisation vessel and placed in oil under atmosphere of cooled N_2 gas. A suitable single crystal was mounted to the end of a glass fibre and placed on a geometer which then placed in the cradle while maintaining the sample at a low temperature. Data collection was performed with an Oxford-Diffraction KUMA equipped with a Sapphire CCD area detector. The radiation source was graphite monochromated Mo–Kα with $\lambda = 0.71073$ Å. The crystal was kept under a gaseous flow of N_2 cooled to 140 K during the entire data collection. The unit cell and orientation matrix was determined by indexing reflections from the entire data set using CrysAlis RED [29]. All data sets are based on collecting reflections for the entire Ewald sphere utilizing the programs CrysAlis CCD [29]. After data integration with CrysAlis RED, a multi-scan absorption correction based on a semi-empirical method was applied using the SCALE3 ABSPACK program integrated as part of the CrysAlias Pro package. Space group determination was performed with the XPREP program [30]. A structure solution based on the direct method algorithm was employed with SHELXS-97 [31]. Afterwards, anisotropic refinement of all non-hydrogen atoms was completed based on a least-squares full-matrix method against F^2 data using SHELXL-97 [31]. Hydrogen atoms were added through geometrically calculated positions and refined as a riding model using a scaled thermal parameter of the connecting atom. Disordered solvates and counter-ions were treated with a split occupancy model and some cases intra-atomic distances were fixed and restrained. The anisotropic thermal parameters of a few carbon atoms located near heavy centres were isotropically restrained, the thermal parameters of one chloroform solvate in **3**.$(PF_6)_2$ was set isotropic due to a high degree of electron disorder within the occupied region. Relevant crystallographic data for both complexes are given in Tables 2–5 and the captions of Figs. 5 and 6 and additional specific details regarding structure refinement are available in the CIF files. Drawings in the paper (Figs. 5 and 6) were produced with the program diamond 3.1e [32]. Further details are available in the CIF files deposited in the CCDC as reference numbers 664732 and 664733.

Table 5 Crystallographic data for **2**.PF_6 and **3**.$(PF_6)_2$

	2.PF_6	**3**.$(PF_6)_2$
Empirical formula	$C_{53}H_{55.12}AuCl_{7.96}F_6P_4Ru$	$C_{114}H_{158}AuCl_{19}F_{12}O_3P_8Pt_3Ru$
Formula weight (g mol^{-1})	1510.37	3609.02
Temperature (K)	140(2)	140(2)
Crystal system	Triclinic	Triclinic
Space group	*P*–1	*P*–1
Crystal characteristics	Orange block	Red prism
Crystal size (mm)	0.31 × 0.23 × 0.18	0.75 × 0.45 × 0.42
a (Å)	12.3039(4)	18.6194(5)
b (Å)	13.8985(4)	18.8750(5)
c (Å)	17.9910(6)	21.8904(5)
a (°)	83.269(3)	65.928(2)
b (°)	86.719(3)	85.770(2)
g (°)	70.912(3)	84.149(2)
V ($Å^3$)	2886.78(16)	6983.2(3)
Z	2	2
r (Mg m^{-3})	1.738	1.716
Absorption coefficient (mm^{-1})	3.335	4.663
Collected, independent reflections	18675	41504
Collection θ range (°)	2.70–25.25	2.74–25.00
Completeness	88.0	87.4
Data	9188	21506
Restraints	54	42
Parameters	738	1526
Goodness-of-fit on F^2	1.025	1.147
R_1 ($I > 2s(I)$), wR_2 ($I > 2s(I)$)	0.0400, 0.0963	0.0642, 0.1639
R_1 (all data), wR_2 (all data)	0.0586, 0.1077	0.0859, 0.1859
Maximum, minimum residual electron density (e $Å^{-3}$)	3.860, −1.109	4.168, −3.651

Acknowledgements This work was supported by the EPFL and the Swiss National Science Foundation. We are grateful to Dr E. Solari for assistance with crystallography. We also thank the New Zealand Foundation for Research, Science and Technology for a Top Achiever Doctoral Fellowship (A. B. C.).

References

1. For example see, (a) P. Braunstein, L. Oro, and P. R. Raithby (eds.), *Metal Clusters in Chemistry* (Wiley-VCH, Weinheim, 1999). (b) P. J. Dyson and J. S. McIndoe (eds.), *Transition Metal Carbonyl Cluster Chemistry* (Gordon and Breach Science Publishers, 2000).
2. P. J. Dyson (1999). *Adv. Organomet. Chem.* **43**, 43. In this review the use of Me_3NO is extensively discussed.
3. (a) W. L. Gladfelter, and G. L. Geoffroy (1980). *Adv. Organomet. Chem.* **18**, 207. (b) L. J. Farrugia (1990). *Adv. Organomet. Chem.* **31**, 301. (c) K. H. Whitmire (1998). *Adv. Organomet. Chem.* **42**, 1.

4. (a) R. D. Adams, B. Captain, W. Fu, and M. D. Smith (2002). *J. Am. Chem. Soc*. **124**, 5628. (b) R. D. Adams, B. Captain, W. Fu, M. B. Hall, J. Manson, M. D. Smith, and C. E. Webster (2004). *J. Am. Chem. Soc*. **126**, 5253. (c) R. D. Adams, B. Captain, P. J. Pellechia, and M. D. Smith (2004). *Inorg. Chem*. **43**, 3921. (d) R. D. Adams, B. Captain, M. B. Hall, J. L. Smith, Jr., and C. E. Webster (2005). *J. Am. Chem. Soc*. **127**, 1007.
5. L. H. Gade (1993). *Angew. Chem. Int. Ed*. **32**, 24.
6. I. D. Salter (1989). *Adv. Organomet. Chem*. **29**, 249.
7. D. G. Evans, D. M. P. Mingos (1982). *J. Organomet. Chem*. **232**, 171.
8. S. W. A. Fong and T. S. A. Hor (1998). *J. Clust. Sci*. **9**, 351.
9. D. S. Shephard, B. F. G. Johnson, A. Harrison, S. Parsons, S. P. Smidt, L. J. Yellowlees, and D. Reed (1998). *J. Organomet. Chem*. **563**, 113.
10. For example, see: (a) E. Louattani, J. Suades, K. Urtiaga, M. I. Arriortua, and X. Solans (1996). *Organometallics* **15**, 468. (b) N. E. Leadbeater, J. Lewis, P. R. Raithby, and A. J. Edwards (1997). *J. Organomet. Chem*. **545–546**, 567. (c) N. T. Lucas, M. P. Cifuentes, L. T. Nguyen, and M. G. Humphrey (2001). *J. Clust. Sci*. **12**, 201. (d) W.-Y. Yeh, C.-I. Li, S.-M. Peng, and G.-H. Lee (2004). *J. Organomet. Chem*. **689**, 105.
11. X. Lei, E. E. Wolf, and T. P. Fehlner (1998). *Eur. J. Inorg. Chem*. 1835.
12. C. Boxwell, P. J. Dyson, D. J. Ellis, and T. Welton (2002). *J. Am. Chem. Soc*. **124**, 9334.
13. A. Moor, P. S. Pregosin, and L. M. Venanzi (1981). *Inorg. Chim. Acta* **48**, 153.
14. D. Imhof, U. Burckhardt, K.-H. Dahmen, F. Joho, and R. Nesper (1997). *Inorg. Chem*. **36**, 1813.
15. Small deviations from the observed and calculated spectra occurs as a result of the difficulty in fitting the $^{1}J_{PtPt'}$ coupling constant. The effected satellites in the observed spectrum have increased line broadening in comparison to the simulation.
16. (a) W. Henderson, J. S. McIndoe, B. K. Nicholson, and P. J. Dyson (1998). *J. Chem. Soc., Dalton Trans*. 519. (b) P. J. Dyson, B. F. G. Johnson, J. S. McIndoe, and P. R. R. Langridge-Smith (2000). *Inorg. Chem*. **39**, 2430.
17. A. R. Timerbaev, C. G. Hartinger, S. S. Aleksenko, and B. K. Keppler (2006). *Chem. Rev*. **106**, 2224.
18. C. G. Hartinger, W. H. Ang, A. Casini, L. Messori, B. K. Keppler, and P. J. Dyson (2007). *J. Anal. At. Spectrom*. **22**, 960.
19. A. Casini, G. Mastrobuoni, W. H. Ang, C. Gabbiani, G. Pieraccini, G. Moneti, P. J. Dyson, and L. Messori (2007). *ChemMedChem* **2**, 631.
20. N. C. Baenziger, W. E. Bennett, and D. M. Soboroff (1976). *Acta Crystallogr., Sect. B: Struct. Crystallogr. Cryst. Chem*. **32**, 962.
21. P. Sevollano, M. E. Garcia, A. Habtemariam, S. Parsons, and P. J. Sadler (1999). *Met.-Based Drugs* **6**, 211.
22. E. J. Fernandez, M. C. Gimeno, P. G. Jones, A. Laguna, M. Laguna, and E. Olmos (1996). *J. Chem. Soc., Dalton Trans*. 3603.
23. P. Sevillano, A. Habtemariam, M. I. G. Seijo, A. Castineiras, S. Parsons, M. E. Garcia, and P. J. Sadler (2000). *Aust. J. Chem*. **53**, 635.
24. C. Mealli (1982). *Acta Crystallogr., Sect. B: Struct. Crystallogr. Cryst. Chem*. **38**, 1040.
25. A. Albinati (1977). *Inorg. Chim. Acta*. **22**, L31.
26. R. Usón and A. Laguna, in R. Bruce and J. J. Eisch (eds.), *Organometallic Syntheses*, vol. 3 (Academic Press, New York, 1986), p. 322.
27. K.-H. Dahmen, A. Moor, R. Naegeli, and L. M. Venanzi (1991). *Inorg. Chem*. **20**, 4285.
28. P. H. M. Budzelaar (1997). *g*-NMR v4.0, IvorySoft.
29. Oxford Diffraction. CrysAlis CCD and CrysAlis RED version 1.71, 2006, Oxford Diffraction Ltd, Abingdon, Oxfordshire, United Kingdom.
30. Bruker-Nonius. XPREP: Reciprocal Space Exploration, version 6.14. 2003, Bruker AXS, Madison, Wisconsin, USA.
31. G. M. Sheldrick, SHELXL-97: A program for the refinement of crystal structures. Release 6. 2003, Institut für Anorganische Chemie der Universität Göttingen, Tammannstr, Germany.
32. Diamond 3.1e, Crystal and Molecular Structure Visualization Program, 2007, Crystal Impact, Bonn, Germany.